

Effects of filling, strain, and electric field on the Néel vector in antiferromagnetic CrSb

In Jun Park,^{1,*} Sohee Kwon,¹ and Roger K. Lake^{1,†}

¹*Laboratory for Terascale and Terahertz Electronics (LATTE),
Department of Electrical and Computer Engineering,
University of California, Riverside, CA 92521, USA*

(Dated: May 9, 2022)

CrSb is a layered antiferromagnet (AFM) with perpendicular magnetic anisotropy, a high Néel temperature, and large spin-orbit coupling (SOC), which makes it interesting for AFM spintronic applications. To elucidate the various mechanisms of Néel vector control, the effects of strain, band filling, and electric field on the magnetic anisotropy energy (MAE) of bulk and thin-film CrSb are determined and analysed using density functional theory. The MAE of the bulk crystal is large (1.2 meV per unit cell). Truncation of the bulk crystal to a thin film consisting of an integer number of unit cells breaks inversion symmetry, creates a large charge dipole and average electric field across the film, and breaks spin degeneracy, such that the thin film becomes a ferrimagnet. The MAE is reduced such that its sign can be switched with realistic strain, and the large SOC gives rise to an intrinsic voltage controlled magnetic anisotropy (VCMA).

I. INTRODUCTION

Antiferromagnetic (AFM) materials are of great interest for future spintronics applications¹. Their resonant frequencies are much higher than those of ferromagnetic (FM) materials, which allows them to be used in the THz applications^{2–4} and ultrafast switching⁵. However, it is challenging to control and detect the antiferromagnetic states. There are several methods to control the spins in AFMs such as via exchange bias with a proximity FM layer⁶ and the use of electric current by Néel spin-orbit torque⁷. The latter method has been extensively studied, although the results have recently been questioned^{8,9}. Controlling the Néel vector without electric current is promising for ultra low power applications, since it has been predicted that magnetization reversal can be achieved with atto joule (aJ) level energy consumption¹⁰. Electric field control of the magnetic properties of AFMs can be realized indirectly through the mechanism of mechanical strain created from a piezoelectric substrate^{11–17} or a combination of strain plus exchange spring¹⁸. It can also be realized directly through the mechanism of voltage controlled magnetic anisotropy (VCMA). This mechanism has been experimentally and theoretically studied for FMs^{19–28}, and the experimental results have been recently reviewed.²⁹ Technological applications have been described and analysed^{30–32}. More recently, several theoretical studies of VCMA of AFMs have been reported^{5,33–35}.

CrSb crystallizes in the hexagonal NiAs-type structure, and the spins on the Cr atoms couple ferromagnetically within the hexagonal plane and antiferromagnetically along the hexagonal axis as shown in Fig. 1. In the ground state, the Néel vector aligns along the hexagonal axis ([0001] direction), so that it has perpendicular magnetic anisotropy (PMA). The bands near the Fermi energy are composed of the d-orbitals of the Cr atoms, and these bands give rise to a large peak in the density of states near the Fermi energy.^{36–39} The Sb atoms pro-

vide significant SOC. CrSb has a high Néel temperature (705 K) making it suitable for on-chip applications⁴⁰. Recently, CrSb has been used to control the magnetic textures and tune the surface states of topological insulators^{41–43}.

We examine three different physical mechanisms that alter the magnetic anisotropy of bulk and thin-film CrSb: (i) strain, (ii) electron filling, and (iii) electric field. Density functional theory (DFT) calculations of the magnetostriction coefficient, strain coefficient, filling coefficient, and VCMA coefficient characterize the effectiveness of the three methods in modifying the MAE.

II. METHODS

We perform first principles calculations as implemented in the Vienna Ab initio Simulation Package (VASP)⁴⁴ to investigate the effects of strain, electric field, and band filling on the magnetic anisotropy of CrSb. Projector augmented-wave (PAW) potentials⁴⁵ and the generalized gradient approximation (GGA) parameterized by Perdew-Burke-Ernzerhof (PBE) are employed⁴⁶. A cut-off energy of 500 eV and $8 \times 8 \times 8$ Γ -centered k-point grid were used to make sure the total energy converged within 10^{-7} eV per unit cell. A GGA+ U implementation was also used to reproduce the magnetic moment on the Cr atom corresponding to the experimental values⁴⁷. We used $U_{eff} = 0.25$ eV for the Cr atom where $U_{eff} = U - J$.

From the initial bulk structure, uniaxial strain along the x -axis is applied and the structure is fully relaxed along y and z axes until all forces on each atom are less than 10^{-3} eV \AA^{-1} . Here, x , y , and z axes are the ones from the Cartesian coordinate system, and the x and z axes are parallel to the a and c axes in the Fig. 1, respectively, since the unit cell is hexagonal. The strain is defined as $\varepsilon = (a - a_0)/a_0 \times 100\%$ where a and a_0 are the lattice constants along x with and without strain, respectively. The calculated lattice constants without strain are $a_0 = 4.189$ \AA and $c_0 = 5.394$ \AA , which are

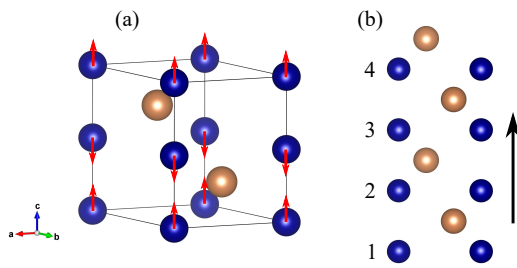


FIG. 1: (a) Bulk antiferromagnetic CrSb crystal structure and spin texture in the ground state. Blue and brown spheres indicate the Cr and Sb atoms, respectively. (b) 1.1 nm thin film with a thickness of 2 unit cells. The numbers index the Cr atoms, and the arrow indicates the direction of positive applied field for VCMA calculations.

close to those from experiment⁴⁷.

To obtain the charge density, a spin-polarized self-consistent calculation is performed with the relaxed structure for each strain. Using the obtained charge densities, the total energies E_{\parallel} and E_{\perp} are calculated in the presence of SOC where E_{\parallel} and E_{\perp} are the total energies with the Néel vector along [1000] and [0001] directions, respectively. The magnetic anisotropy energy (MAE) is defined as $E_{\text{MAE}} = E_{\parallel} - E_{\perp}$. For uniformity in comparison between bulk and thin-film structures, all values of E_{MAE} are reported per bulk unit cell (u.c.) (i.e. per two Cr atoms). For MAE calculations, a denser k-point grid ($16 \times 16 \times 16$) is used for accuracy. The same procedures are performed to investigate the effect of electron filling on the MAE, and the structures are optimized for each number of electrons in the unit cell.

Charge transfer between the Cr and Sb ions is analyzed by calculating the Bader charges.⁴⁸ The “net charge” on each atom is defined as the number of valence electrons for a given atom minus the Bader charge on the atom. The Bader charges are used to understand the effect of truncation of the bulk to a slab and the application of an electric field. Volumetric charge densities (ρ_v) at different electric fields are also calculated from the spin-polarized calculation. The difference between them is plotted to understand the charge transfer induced by the electric field over the slab.

To investigate the effect of strain and electric field on the MAE of thin-film CrSb, we consider slab structures consisting of 2 and 3 unit cells along the c -axis (~ 1.1 nm and 1.6 nm). A 15 Å vacuum layer is included. The stability of two different surface terminations is quantified by calculating the cohesive energy defined as $E_{\text{coh}} = (E_{\text{crystal}} - E_{\text{isolated}})/N$ where N is the total number of atoms, E_{crystal} is the total energy of the relaxed slab structure, and E_{isolated} is the sum of the energies of the individual atoms. For the thin-film structures, a $23 \times 23 \times 1$ Γ -centered k-point grid with a 500 eV cutoff energy is used to ensure the same convergence

criteria as the bulk structure. The structures are fully relaxed until all forces on each atom are less than 10^{-3} eV Å $^{-1}$ without changing the volume. Vertical external electric fields are applied to the slab by introducing a dipole layer in the middle of the vacuum layer. The dipole layer also corrects for the built in dipole moment in the CrSb slab structures to prevent interactions between the artificial periodic images^{49,50}. The equilibrium charge density is obtained by performing a spin-polarized self-consistent calculation without the electric field. Then, the charge densities with increasing applied electric fields along c -axis are obtained by relaxing the charges from the calculation with the previous electric field. For each electric field, the MAE is calculated using a $46 \times 46 \times 1$ k-point grid.

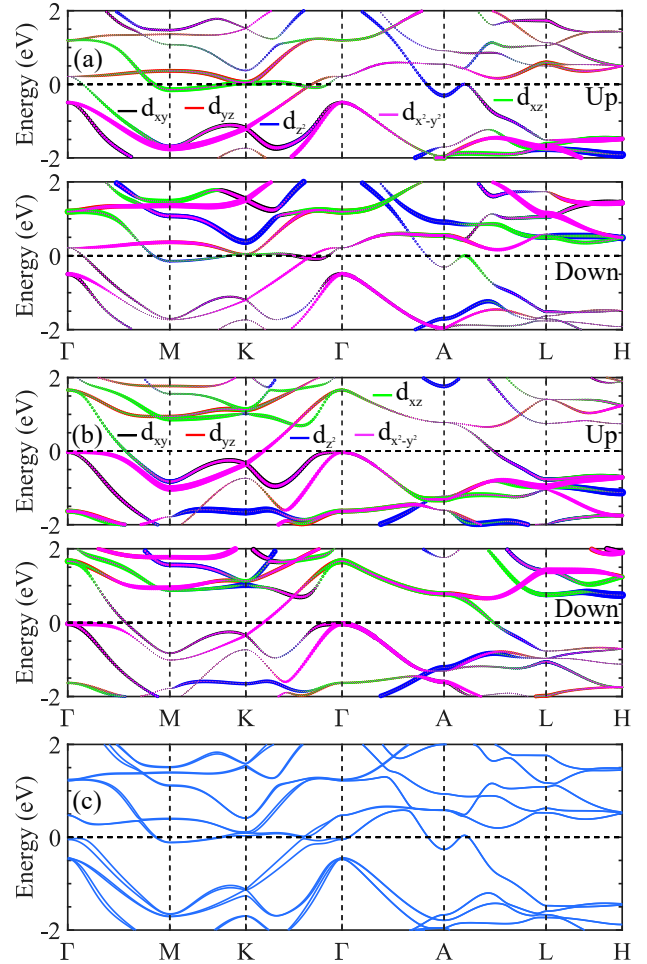


FIG. 2: The d-orbital resolved bandstructures (without SOC) of bulk CrSb when the electron number is (a) 22 (equilibrium) and (b) 21. For both (a) and (b), the top panel is for spin up, and the bottom panel is for spin down. The colors indicate the different d-orbitals, as indicated by the legends. (c) The bandstructure of CrSb in equilibrium with SOC.

III. RESULTS AND DISCUSSION

In Fig. 2, the electronic bandstructure of bulk CrSb is shown. Fig. 2(a) is the d-orbital resolved bandstructure for a Cr atom in equilibrium in the absence of SOC. The colors denote different orbitals as indicated by the legends, and the line thicknesses denote the relative occupations. The spin-up bands are shown in the top panel, and the spin-down bands are shown in the bottom panel. Fig. 2(c) shows the equilibrium bandstructure in the presence of SOC.

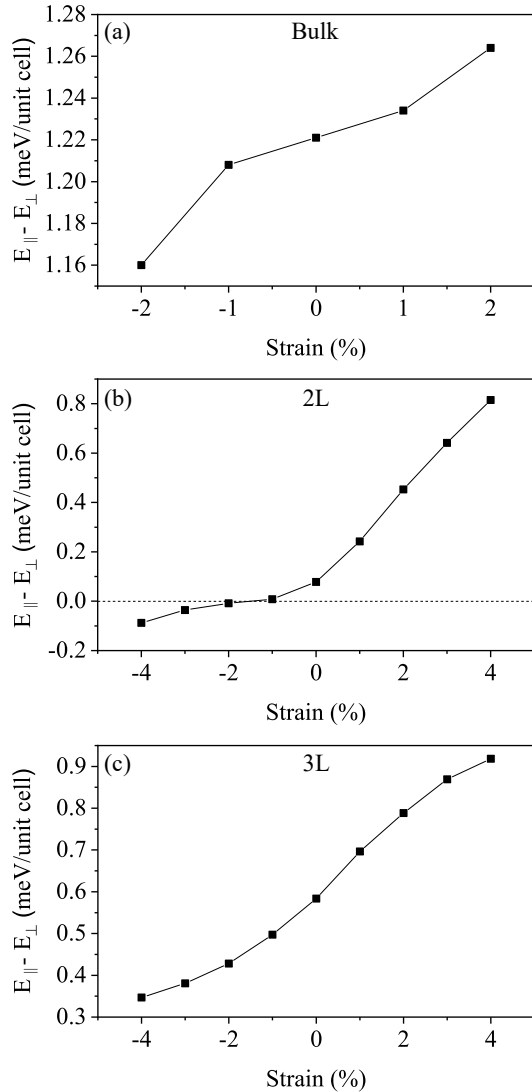


FIG. 3: MAE as a function of applied strain of (a) the bulk crystal, the (b) 1.1 nm, and (c) 1.6 nm thin films.

The effect of spin-orbit coupling (SOC) on the bandstructure is relatively large. A comparison of Fig. 2(a) to 2(c) shows that the SOC breaks the spin degeneracy throughout much of the Brillouin zone and creates anti-crossings at a number of band-crossing points. The largest band splitting occurs at Γ . The two bands that

touch at 0.2 eV in the absence of SOC are split by ~ 0.5 eV and the hole like band is pushed down below E_F .

There is also significant electron transfer from the Cr atoms to the Sb atoms. The calculated Bader charges show a charge transfer of approximately 0.5 electrons from the Cr to the Sb atoms, and this transfer is identical for all Cr and Sb atoms in the bulk crystal. This corresponds to alternating sheet carrier concentrations of $\pm 3.3 \times 10^{14} \text{ cm}^{-2}$ on alternating Cr and Sb layers.

Fig. 3(a) shows the MAE as a function of applied strain for bulk CrSb. The value at zero strain is $E_{\text{MAE}} = 1.2 \text{ meV/u.c.}$ The positive sign of the MAE indicates that the Néel vector aligns along the c-axis (out-of-plane) independent of the strain. The monotonic increase in the MAE indicates that CrSb behaves like a magnet with a negative magnetostriction coefficient, since the tensile strain favors out-of-plane anisotropy. The magnetostriction coefficient (λ_s) is defined as

$$\lambda_s(\text{ppm}) = -\frac{2K_{\text{me}}(1-v^2)}{3E\varepsilon}, \quad (1)$$

where v , E , and ε are the Possion's ratio (0.288), Young's modulus (78.3 GPa), and strain, respectively⁵¹. The magnetoelastic anisotropy constant, K_{me} , is calculated from the difference between two MAEs with and without strain (*i.e.*, $\text{MAE}(\varepsilon) - \text{MAE}(0)$). The parameters v and E are taken from a previous study⁵². The calculated λ_s for small strain (between -1 % to 1 %) is -19.8 ppm. CrSb has a negative value of λ_s , and the magnitude of λ_s is similar to that of MnNi and MnPd¹³. We also define a strain coefficient as $\alpha_{\varepsilon} = dE_{\text{MAE}}/d\varepsilon$ evaluated at $\varepsilon = 0$. The value for bulk CrSb is $\alpha_{\varepsilon} = 0.013 \text{ meV}/\%\text{strain}$.

The response of the bulk MAE as a function of the electron number in the unit cell is shown in Fig. 4. In equilibrium, the unit cell has 22 valence electrons, which is denoted by the vertical line in the figure. The MAE decreases most rapidly when the CrSb is depleted, and it changes sign when the hole doping reaches 0.75/u.c. For electron depletion, the filling coefficient, defined as $\alpha_n = dE_{\text{MAE}}/dn$, is 2.92 meV / electron / u.c.

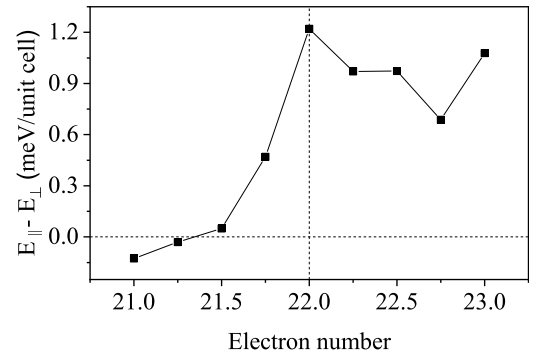


FIG. 4: MAE of bulk crystal versus the number of electrons in the unit cell.

To understand the physical origin of the transition due to charge depletion, we consider the d-orbital resolved

band structures for a Cr atom plotted for 2 different electron numbers in the unit cell, 22 (equilibrium) in Fig. 2(a) and 21 in Fig. 2(b). Within second-order perturbation theory, the MAE is approximately expressed as⁵³

$$MAE \propto \xi^2 \sum_{o,u} \frac{|\langle \Psi_o^\uparrow | \hat{L}_z | \Psi_u^\uparrow \rangle|^2 - |\langle \Psi_o^\uparrow | \hat{L}_{x(y)} | \Psi_u^\uparrow \rangle|^2}{E_u^\uparrow - E_o^\uparrow} \\ + \xi^2 \sum_{o,u} \frac{|\langle \Psi_o^\downarrow | \hat{L}_z | \Psi_u^\downarrow \rangle|^2 - |\langle \Psi_o^\downarrow | \hat{L}_{x(y)} | \Psi_u^\downarrow \rangle|^2}{E_u^\downarrow - E_o^\downarrow} \\ + \xi^2 \sum_{o,u} \frac{|\langle \Psi_o^\uparrow | \hat{L}_{x(y)} | \Psi_u^\downarrow \rangle|^2 - |\langle \Psi_o^\uparrow | \hat{L}_z | \Psi_u^\downarrow \rangle|^2}{E_u^\downarrow - E_o^\uparrow}, \quad (2)$$

where $\Psi_o(\Psi_u)$, $E_o(E_u)$, and ξ are the (un)occupied states, (un)occupied eigenvalues, and the spin-orbit coupling constant, respectively. \hat{L}_z and $\hat{L}_{x(y)}$ are the out-of plane and in-plane components of the orbital angular momentum operator, and \uparrow and \downarrow denote spin-up and spin-down. The non-zero matrix elements in the Eq. (2) are $\langle d_{xz} | \hat{L}_z | d_{yz} \rangle$, $\langle d_{x^2-y^2} | \hat{L}_z | d_{xy} \rangle$, $\langle d_{z^2} | \hat{L}_x | d_{yz} \rangle$, $\langle d_{xy} | \hat{L}_x | d_{xz} \rangle$, $\langle d_{x^2-y^2} | \hat{L}_x | d_{yz} \rangle$, $\langle d_{z^2} | \hat{L}_y | d_{xz} \rangle$, $\langle d_{xy} | \hat{L}_y | d_{yz} \rangle$, and $\langle d_{x^2-y^2} | \hat{L}_y | d_{xz} \rangle$. The largest contributions to Eq. (2) come from pairs of nearly degenerate occupied and unoccupied states near the Fermi level. In equilibrium (Fig. 2(a)), the main contributions to the MAE come from the spin-orbit coupling between occupied d_{xz}^\uparrow and unoccupied d_{yz}^\uparrow states at the K point and near the Γ point, and between occupied d_{xy}^\downarrow and unoccupied $d_{x^2-y^2}^\downarrow$ states near Γ point. All of these states couple through the \hat{L}_z operator, which results in the positive MAE value (out-of-plane anisotropy). When CrSb is depleted (see Fig. 2(b)), the entire band structure moves upward so that the main contributor states of the perpendicular anisotropy become unoccupied. This reduces the value of the MAE, and eventually reverses the sign for $n = 21.25$.

We now consider thin-film slabs with thicknesses of 2 and 3 unit cells corresponding to 1.1 nm and 1.6 nm, respectively. For the thinner slab, the cohesive energies are calculated for a 7 atomic layer structure of alternating Cr and Sb layers terminated on both ends with a Cr layer and for a 8 atomic layer structure (2 unit cells) terminated on one end with Cr and on the other with Sb. The cohesive energies of the 7 and 8 atomic layer structures are -3.328 eV and -3.517 eV, respectively. For the thicker slab, cohesive energies are calculated for a 11 atomic layer structure and a 12 atomic layer structure, and the cohesive energies are -3.522 eV and -3.636 eV, respectively. Thus, the slab structures with integer number of unit cells are the most stable, and they are the ones that we will consider.

With these thin-film structures, inversion symmetry is broken, since one end is terminated with a Cr layer and the other end is terminated with a Sb layer. Thus, these thin films are Janus structures. The two unit cell thin-film is shown in Fig. 1(b). Below, results for strain and VCMA coefficients are presented for both the 2 and 3 unit

cell thin-films, and the in-depth microscopic analysis of the charge, magnetic moments, and electronic structure focuses on the 2 unit cell thin-film.

In the thin films, there is a net polarization of electron charge between the positively charged Cr layer on the bottom and the negatively charged Sb layer on the top. The excess charge on each atom in the bulk and in the 2 unit-cell slab is shown in Fig. 5(a,b), and it is clear that, in the slab, the charge transfer is no longer balanced layer-by-layer. The net charge polarization gives rise to a built-in electric field that alternates positively and negatively within the slab, but, its average value points from the positive Cr layer to the negative Sb layer parallel to the applied field shown in Fig. 1(b). Treating the Bader charges as sheet charges, the average electric field in the slab is 9.1×10^7 V/cm, and the average potential difference across the slab of 8.6 V.

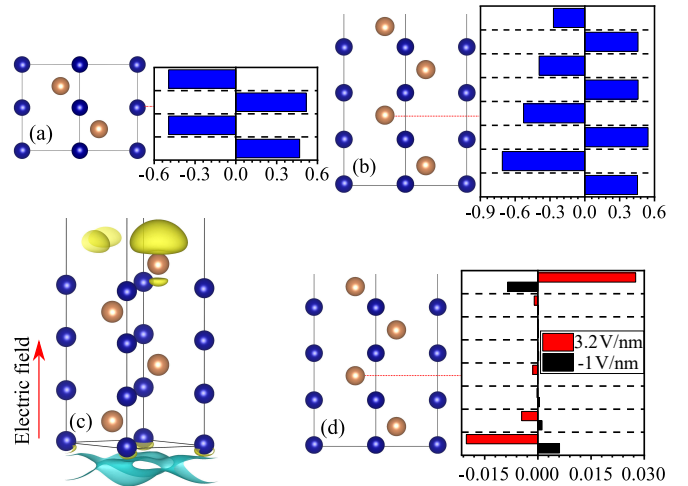


FIG. 5: The net charges on the Cr and Sb atoms, in units of $|e|$, of (a) bulk and (b) 1.1 nm thin film CrSb in equilibrium. (c) The change of charge induced by an applied electric field. The charge density change is calculated by subtracting the charge density at the electric field of -1 V/nm from that at 3.2 V/nm (i.e., $\rho_v(3.2 \text{ V/nm}) - \rho_v(-1 \text{ V/nm})$). Blue indicates negative charge and yellow indicates positive charge. (d) Change in Bader charges induced by the electric field (indicated in the legend) with the reference charge taken from equilibrium charges shown in (b).

The truncation of the bulk to a finite slab results not only in a loss of *local* balance between the positive and negative charges, but also in a *global* imbalance of the magnetic moments of the Cr ions. In other words, the cancellation of magnetic moments between alternating layers of Cr is no longer exact, and a small net magnetic moment exists in the slab. The magnetic moments on each Cr atom are listed in Table I with the numbering corresponding to that shown in Fig. 1(b). The magnitudes of the magnetic moments in the Cr layers monotonically decrease from bottom to top as the Cr atoms approach the Sb terminated end of the slab. The breaking of the spin degeneracy is readily apparent in

the bandstructure of the slab shown in Fig. 6(a). The degeneracy between the up-spin and down-spin bands is broken, and the CrSb slab has become a ferrimagnet.

TABLE I: Magnetic moment for each Cr atom in the bulk and the 1.1 nm thin-film with spin-orbit coupling. The indices on the Cr atoms correspond to those in Fig. 1.

Atom	$\mu_{Cr,bulk}$ (μ_B)	$\mu_{Cr,2L}$ (μ_B)
Cr ₁	3.035	3.763
Cr ₂	-3.035	-3.190
Cr ₃		3.116
Cr ₄		-2.889

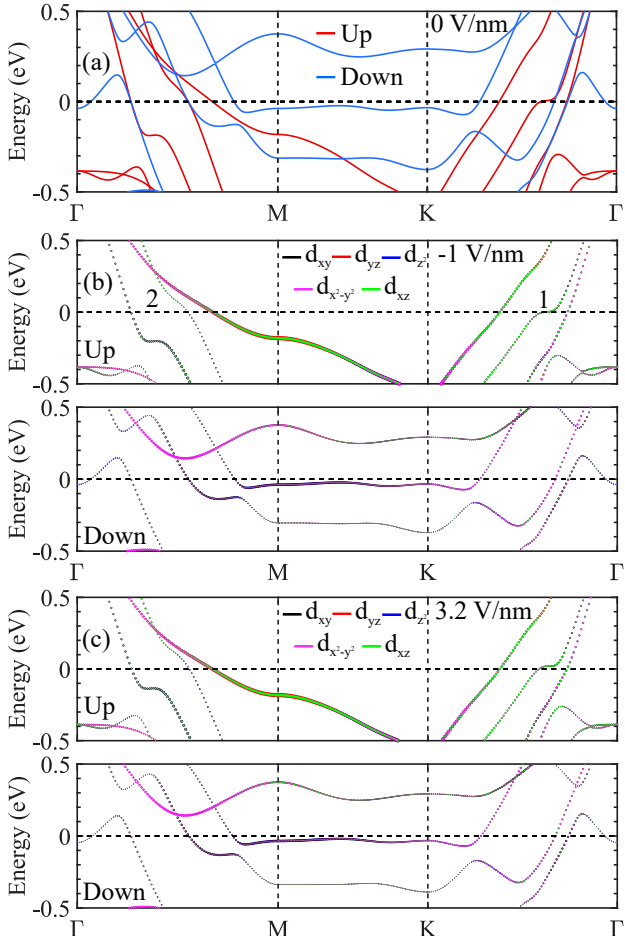


FIG. 6: (a) Spin resolved bandstructure of the 1.1 nm CrSb thin-film in equilibrium. (b,c) The d-orbital resolved bandstructures of the 1.1 nm CrSb thin-film under electric fields of (b) -1 V/nm and (c) 3.2 V/nm. The line colors indicate the d-orbital composition as given by the legends, and the line thicknesses indicate the relative weights.

A third result of truncating the bulk to a slab is that the MAE decreases. For the 1.1 nm slab, the MAE is reduced by a factor of 15 from 1.2 meV/u.c. to 0.079 meV/u.c. (0.17 erg/cm²), and for the 1.6 nm slab, the MAE is reduced by a factor of 2.1 to 0.58 meV/u.c. (1.85

erg/cm²). Also, the sensitivity of the MAE to strain increases. The strain coefficients of the 1.1 and 1.6 nm slabs (α_ε) increase from 0.013 meV/%strain in the bulk to 0.12 meV/%strain and 0.1 meV/%strain, respectively, where the energies are per bulk unit cell (2 Cr atoms). The combined result of the reduced MAE and increased strain coefficient is that a 1.5% uniaxial compressive strain along [1000] direction in the 1.1 nm thin film causes a 90° rotation of the Néel vector from out-of-plane to in-plane as shown in Fig. 3(b).

A fourth result is that the MAE also becomes sensitive to an external electric field as shown in Fig. 7. In other words, the thin slab exhibits intrinsic VCMA. Typically VCMA is found when a magnetic layer is placed in contact with a heavy-metal layer that provides SOC. However, the Sb layers provide large SOC, and the terminating Sb layer serves as the HM layer, such that the CrSb slab has intrinsic VCMA. The MAE decreases linearly as the electric field is increased, and, for the 1.1 nm slab, it changes sign at 3.2 V/nm, which indicates that the Néel vector rotates 90° from out-of-plane to in-plane.

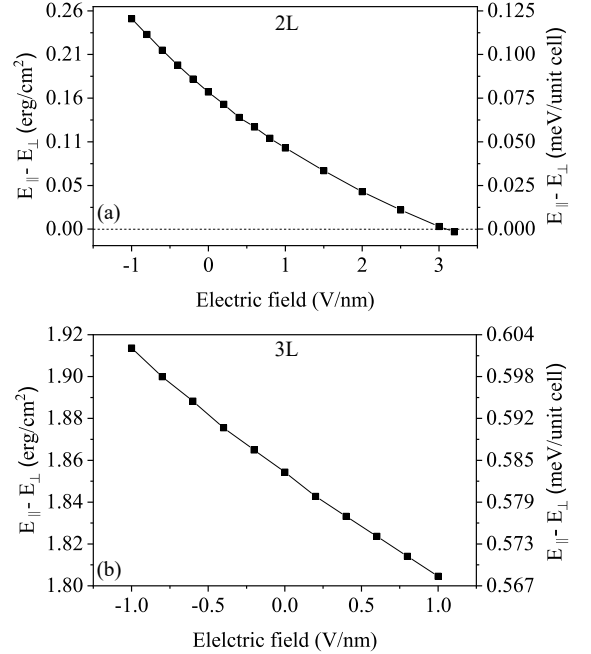


FIG. 7: MAEs of (a) 1.1 nm and (b) 1.6 nm films as a function of applied electric field.

The sensitivity of the MAE to the applied electric field is given by the VCMA coefficient defined as

$$\beta = \frac{\Delta MAE}{\Delta \mathcal{E}_I} = \frac{\Delta MAE}{\Delta \mathcal{E}_{\text{ext}}/\epsilon_I}, \quad (3)$$

where \mathcal{E}_{ext} is the external electric field and \mathcal{E}_I and ϵ_I are the electric field and the relative dielectric constant in the insulator, respectively. In a typical experiment, the insulator would be an oxide layer. In our case, the insulator is the vacuum, so that $\epsilon_I = 1$ and $\mathcal{E}_I = \mathcal{E}_{\text{ext}}$. The values of β , evaluated at $\mathcal{E}_{\text{ext}} = 0$ V/nm, are -76.8

$\text{fJV}^{-1}\text{m}^{-1}$ for the 1.1 nm film and $-55.6 \text{ fJV}^{-1}\text{m}^{-1}$ for the 1.6 nm slab. For comparison, calculated magnitudes of β for a G-AFM FeRh/MgO bilayer range from 130 to 360 $\text{fJ}/(\text{Vm})$ depending on the sign of the electric field, the strain, and the termination layer of either Fe or Rh³³.

To understand which Cr atoms contribute to the VCMA effect, we inspect the change of the orbital magnetic moments and the charge of the Cr atoms in response to the applied field. The difference in the orbital magnetic moments (Δm_l) for each Cr atom in the 1.1 nm slab at different electric fields is calculated and shown in the Table II. Δm_l is defined as $\Delta m_l = m_{l,\perp} - m_{l,\parallel}$, where $m_{l,\perp}$ and $m_{l,\parallel}$ are the orbital magnetic moments with the Néel vector along [0001] and [1000] directions, respectively. The electric field changes Δm_l on Cr_1 by $3 \times 10^{-3} \mu_B$ and on Cr_4 by $1 \times 10^{-3} \mu_B$. The interior atoms show negligible change. The change in charge with applied electric field, plotted in Fig. 5(c,d), shows that, among the Cr atoms, the only significant change in charge occurs on Cr_1 . This is to be expected, since the electric field is screened by the first and last layers from the interior of the CrSb metal. An external field of $\mathcal{E}_{\text{ext}} = 3.2 \text{ V/nm}$ induces a negative charge on Cr_1 of 0.018 electrons, as shown in Fig. 5(d). Both the change in orbital moment and the change in charge with applied electric field suggest that it is reasonable to focus on the Cr_1 atom for further discussion.

TABLE II: Δm_l (in μ_B) for the applied electric fields of -1 V/nm and 3.2 V/nm for each Cr atom in the 1.1 nm slab.

	E-field -1 V/nm	3.2 V/nm
Cr_1	0.003	0
Cr_2	-0.007	-0.007
Cr_3	0.013	0.013
Cr_4	-0.031	-0.030

To elucidate the physical origin of switching mechanism, the d-orbital resolved band structures for the Cr_1 atom under different electric fields are plotted in Fig. 6(b,c). At the electric field of -1 V/nm , the major contribution of the perpendicular anisotropy comes from the spin-orbit coupling between the unoccupied d_{xz}^\uparrow and occupied $d_{x^2-y^2}^\downarrow$ states through \hat{L}_y operator in the region 1. Although the states in the region 1 are coupled through the in-plane angular momentum operator, the contribution of the MAE is positive since they are from different spin channels. In the region 2, the occupied d_{xy}^\uparrow states are coupled with unoccupied d_{xz}^\uparrow states through \hat{L}_x , which contributes the in-plane anisotropy. As the

external field increases (see Fig. 6 (b)), the unoccupied d_{xz}^\uparrow states in the region 1 move away from the Fermi level by 18 meV, which results in the reduction of the out-of-plane anisotropy since the denominator in the Eq. 2 increases. On the other hand, in the region 2, the occupied d_{xy}^\uparrow states move closer to the Fermi energy by 67 meV as the electric field increases so that the in-plane anisotropy increases.

IV. SUMMARY AND CONCLUSIONS

The effects of strain, band filling, and electric field on the MAE of bulk and thin-film CrSb are determined and analysed. The magnitude of the bulk magnetostriction coefficient is comparable with those from other antiferromagnets and ferromagnets, however the MAE is large (1.2 meV/u.c.) and its sign cannot be changed by strain for bulk material. For bulk CrSb, depleting the electron density by 0.75 electrons per unit cell depletes the flat, nearly-degenerate d-orbital bands near the Fermi energy and causes a 90° rotation of the Néel vector from out-of-plane to in-plane. Truncation of the bulk crystal to a thin film breaks inversion symmetry, creates a large charge dipole and potential difference across the slab, and breaks spin degeneracy such that the CrSb slab becomes a ferrimagnet. For the 1.1 nm (1.6 nm) slab, the MAE is reduced from 1.2 meV/u.c. to 0.079 meV/u.c. (0.58 meV/u.c) and the strain coefficient is increased from 0.013 meV/%strain to 0.12 meV/%strain (0.1 meV/%strain). As a result of the reduced MAE and increased strain coefficient, the sign of the MAE in the 1.1 nm slab can be switched with 1.5% uniaxial compressive strain. The large SOC from the Sb combined with broken inversion symmetry of a thin film results in an intrinsic VCMA. The calculated VCMA coefficients for the free-standing 1.1 nm and 1.6 nm thin films with vacuum as the insulator are $-76.8 \text{ fJV}^{-1}\text{m}^{-1}$ and $-55.6 \text{ fJV}^{-1}\text{m}^{-1}$, respectively.

Acknowledgements: This work was supported as part of Spins and Heat in Nanoscale Electronic Systems (SHINES) an Energy Frontier Research Center funded by the U.S. Department of Energy, Office of Science, Basic Energy Sciences under Award DE-SC0012670. This work used the Extreme Science and Engineering Discovery Environment (XSEDE)⁵⁴, which is supported by National Science Foundation Grant No. ACI-1548562 and allocation ID TG-DMR130081.

* ipark008@ucr.edu

† rlake@ece.ucr.edu

¹ V. Baltz, A. Manchon, M. Tsoi, T. Moriyama, T. Ono, and Y. Tserkovnyak, Rev. Mod. Phys. **90**, 015005 (2018).

² T. Jungwirth, X. Marti, P. Wadley, and J. Wunderlich, Nature Nanotechnology **11**, 231 (2016).

³ E. V. Gomonay and V. M. Loktev, Low Temperature Physics **40**, 17 (2014).

⁴ F. Keffer and C. Kittel, *Physical Review* **85**, 329 (1952).

⁵ V. Lopez-Dominguez, H. Almasi, and P. K. Amiri, *Physical Review Applied* **11**, 024019 (2019).

⁶ J. Nogués and I. K. Schuller, *Journal of Magnetism and Magnetic Materials* **192**, 203 (1999).

⁷ P. Wadley, B. Howells, J. Železný, C. Andrews, V. Hills, R. P. Campion, V. Novák, K. Olejník, F. Maccherozzi, S. S. Dhesi, *et al.*, *Science* **351**, 587 (2016).

⁸ C. C. Chiang, S. Y. Huang, D. Qu, P. H. Wu, and C. L. Chien, *Phys. Rev. Lett.* **123**, 227203 (2019).

⁹ A. Churikova, D. Bono, B. Neltner, A. Wittmann, L. Scipioni, A. Shepard, T. Newhouse-Illige, J. Greer, and G. S. D. Beach, *Applied Physics Letters* **116**, 022410 (2020).

¹⁰ Y. G. Semenov, X.-L. Li, and K. W. Kim, *Physical Review B* **95**, 014434 (2017).

¹¹ A. Barra, J. Domann, K. W. Kim, and G. Carman, *Physical Review Applied* **9**, 034017 (2018).

¹² H. Yan, Z. Feng, S. Shang, X. Wang, Z. Hu, J. Wang, Z. Zhu, H. Wang, Z. Chen, H. Hua, *et al.*, *Nature Nanotechnology* **14**, 131 (2019).

¹³ I. J. Park, T. Lee, P. Das, B. Debnath, G. P. Carman, and R. K. Lake, *Applied Physics Letters* **114**, 142403 (2019).

¹⁴ X. Chen, X. Zhou, R. Cheng, C. Song, J. Zhang, Y. Wu, Y. Ba, H. Li, Y. Sun, Y. You, *et al.*, *Nature materials* **18**, 931 (2019).

¹⁵ X. Wang, Z. Feng, P. Qin, H. Yan, X. Zhou, H. Guo, Z. Leng, W. Chen, Q. Jia, Z. Hu, *et al.*, *Acta Materialia* **181**, 537 (2019).

¹⁶ D. Boldrin, A. P. Mihai, B. Zou, J. Zemen, R. Thompson, E. Ware, B. V. Neamtu, L. Ghivelde, B. Esser, D. W. McComb, *et al.*, *ACS applied materials & interfaces* **10**, 18863 (2018).

¹⁷ Z. Liu, H. Chen, J. Wang, J. Liu, K. Wang, Z. Feng, H. Yan, X. Wang, C. Jiang, J. Coey, *et al.*, *Nature Electronics* **1**, 172 (2018).

¹⁸ C. Feng, Y. Li, L. Wang, Y. Cao, M. Yao, F. Meng, F. Yang, B. Li, K. Wang, and G. Yu, *Advanced Functional Materials* **30**, 1909708 (2020).

¹⁹ M. K. Niranjan, C.-G. Duan, S. S. Jaswal, and E. Y. Tsymbal, *Applied Physics Letters* **96**, 222504 (2010).

²⁰ P. K. Amiri and K. L. Wang, in *Spin*, Vol. 2 (World Scientific, 2012) p. 1240002.

²¹ J. G. Alzate, P. Khalili Amiri, G. Yu, P. Upadhyaya, J. A. Katine, J. Langer, B. Ocker, I. N. Krivorotov, and K. L. Wang, *Applied physics letters* **104**, 112410 (2014).

²² P. V. Ong, N. Kioussis, D. Odkhuu, P. Khalili Amiri, K. L. Wang, and G. P. Carman, *Phys. Rev. B* **92**, 020407 (2015).

²³ T. Nozaki, A. Kozioł-Rachwał, W. Skowroński, V. Zayets, Y. Shiota, S. Tamaru, H. Kubota, A. Fukushima, S. Yuasa, and Y. Suzuki, *Phys. Rev. Applied* **5**, 044006 (2016).

²⁴ J. Zhang, P. V. Lukashev, S. S. Jaswal, and E. Y. Tsymbal, *Phys. Rev. B* **96**, 014435 (2017).

²⁵ Z. Wen, H. Sukegawa, T. Seki, T. Kubota, K. Takanashi, and S. Mitani, *Scientific reports* **7**, 45026 (2017).

²⁶ S. Kwon, Q. Sun, F. Mahfouzi, K. L. Wang, P. K. Amiri, and N. Kioussis, *Phys. Rev. Applied* **12**, 044075 (2019).

²⁷ S. Kwon, P.-V. Ong, Q. Sun, F. Mahfouzi, X. Li, K. L. Wang, Y. Kato, H. Yoda, P. K. Amiri, and N. Kioussis, *Physical Review B* **99**, 064434 (2019).

²⁸ T. Nozaki, M. Endo, M. Tsujikawa, T. Yamamoto, T. Nozaki, M. Konoto, H. Ohmori, Y. Higo, H. Kubota, A. Fukushima, *et al.*, *APL Materials* **8**, 011108 (2020).

²⁹ S. Miwa, M. Suzuki, M. Tsujikawa, T. Nozaki, T. Nakamura, M. Shirai, S. Yuasa, and Y. Suzuki, *Journal of Physics D: Applied Physics* **52**, 063001 (2018).

³⁰ K. L. Wang, H. Lee, and P. Khalili Amiri, *IEEE Transactions on Nanotechnology* **14**, 992 (2015).

³¹ W. Kang, Y. Ran, Y. Zhang, W. Lv, and W. Zhao, *IEEE Transactions on Nanotechnology* **16**, 387 (2017).

³² W. Kang, Y. Ran, W. Lv, Y. Zhang, and W. Zhao, *IEEE Magnetics Letters* **7**, 1 (2016).

³³ G. Zheng, S.-H. Ke, M. Miao, J. Kim, R. Ramesh, and N. Kioussis, *Scientific reports* **7**, 1 (2017).

³⁴ Y. Su, M. Li, J. Zhang, J. Hong, and L. You, *Journal of Magnetism and Magnetic Materials* **505**, 166758 (2020).

³⁵ P.-H. Chang, W. Fang, T. Ozaki, and K. Belashchenko, *arXiv preprint arXiv:2008.03249* (2020).

³⁶ J. Dijkstra, C. Van Bruggen, C. Haas, and R. de Groot, *Journal of Physics: Condensed Matter* **1**, 9163 (1989).

³⁷ T. Ito, H. Ido, and K. Motizuki, *Journal of Magnetism and Magnetic Materials* **310**, e558 (2007).

³⁸ L. Kahal, A. Zaoui, and M. Ferhat, *Journal of Applied Physics* **101**, 093912 (2007).

³⁹ S. Polesya, G. Kuhn, S. Mankovsky, H. Ebert, M. Regus, and W. Bensch, *Journal of Physics: Condensed Matter* **24**, 036004 (2011).

⁴⁰ W. Takei, D. E. Cox, and G. Shirane, *Physical Review* **129**, 2008 (1963).

⁴¹ Q. L. He, X. Kou, A. J. Grutter, G. Yin, L. Pan, X. Che, Y. Liu, T. Nie, B. Zhang, S. M. Disseler, B. J. Kirby, W. Ratcliff II, Q. Shao, K. Murata, X. Zhu, G. Yu, Y. Fan, M. Montazeri, X. Han, J. A. Borchers, and K. L. Wang, *Nature Materials* **16**, 94 (2017).

⁴² Q. L. He, G. Yin, L. Yu, A. J. Grutter, L. Pan, C.-Z. Chen, X. Che, G. Yu, B. Zhang, Q. Shao, A. L. Stern, B. Casas, J. Xia, X. Han, B. J. Kirby, R. K. Lake, K. T. Law, and K. L. Wang, *Phys. Rev. Lett.* **121**, 096802 (2018).

⁴³ T. Wang, D. Gao, and M. Si, *Japanese Journal of Applied Physics* **58**, 080910 (2019).

⁴⁴ G. Kresse and J. Hafner, *Physical Review B* **47**, 558 (1993).

⁴⁵ P. E. Blöchl, *Physical Review B* **50**, 17953 (1994).

⁴⁶ J. P. Perdew, K. Burke, and M. Ernzerhof, *Physical Review Letters* **77**, 3865 (1996).

⁴⁷ A. I. Snow, *Phys. Rev.* **85**, 365 (1952).

⁴⁸ G. Henkelman, A. Arnaldsson, and H. Jónsson, *Computational Materials Science* **36**, 354 (2006).

⁴⁹ J. Neugebauer and M. Scheffler, *Physical Review B* **46**, 16067 (1992).

⁵⁰ G. Makov and M. Payne, *Physical Review B* **51**, 4014 (1995).

⁵¹ G. Yu, Z. Wang, M. Abolfath-Beygi, C. He, X. Li, K. L. Wong, P. Nordeen, H. Wu, G. P. Carman, X. Han, I. A. Alhomoudi, P. K. Amiri, and K. L. Wang, *Applied Physics Letters* **106**, 072402 (2015).

⁵² Z. Charifi, D. Guendouz, H. Baaziz, F. Soyalp, and B. Hamad, *Physica Scripta* **94**, 015701 (2018).

⁵³ D.-s. Wang, R. Wu, and A. J. Freeman, *Phys. Rev. B* **47**, 14932 (1993).

⁵⁴ J. Towns, T. Cockerill, M. Dahan, I. Foster, K. Gaither, A. Grimshaw, V. Hazlewood, S. Lathrop, D. Lifka, G. D. Peterson, *et al.*, *Computing in Science & Engineering* **16**, 62 (2014).